Draft version December 7, 2011
Preprint typeset using LaTeX style emulateapj v. 08/13/06

PARALLEL 3D MONTE CARLO DUST RADIATIVE TRANSFER ON GPU

Frank Heymann
Department of Physics and Astronomy, University of Kentucky, Lexington, KY 40506-0055, USA
European Southern Observatory (ESO), Karl-Schwarzschild-Str. 2, 85748 Garching, Germany and
Astronomisches Institut, Ruhr-University, Bochum, Germany

and

Ralf Siebenmorgen
European Southern Observatory (ESO), Karl-Schwarzschild-Str. 2, 85748 Garching, Germany

Draft version December 7, 2011

ABSTRACT

A three dimensional parallel Monte Carlo dust radiative transfer code is presented. To overcome the huge computing time requirements of Monte Carlo treatments, the computational power of vectorized hardware is used either utilizing multi–core computer power or graphics processing units. The approach is a self-consistent way to solve the radiative transfer equation and calculate dust temperatures and scattering events in arbitrary three dimensional configurations. The spectral energy distribution (SED) of the object is derived at low spatial resolution by a photon counting procedure and at high spatial resolution by a ray–tracer. The latter method allows to compute noise free images of the objects at any frequencies and arbitrary viewing angles. We test the robustness of our approach against other radiative transfer codes. The SED and dust temperatures of one or two dimensional benchmarks are reproduced at high precision. In addition different Monte Carlo optimization algorithms are analyzed and their capability of parallelization is discussed. The code is applied to model the appearance of AGN at optical and infrared wavelengths. A clumpy AGN torus model is presented, in which grains are fluffy composites of silicate and carbon. The dependence of the SED of the AGN by varying the number of clumps in the torus or the viewing angle is studied. The appearance of the 10μm silicate absorption and emission features is discussed in the context of the model. The clumpy torus is used to fit the SED of the radio loud quasar 3C249.1 for which a cirrus component is required to account for the far infrared emission.

Subject headings: test

1. INTRODUCTION

Dust obscured objects cannot be studied directly in the UV/optical, since the dust shields most of the visible light. To derive the UV/optical component or to constrain the morphological structure from available near/far infrared data, a detailed model of the interaction of photons with the dust is required. The problem is to solve the radiative transfer (RT) equation. Analytically, this can only be done in some simple configurations, for example by assuming spherical or disk symmetry in which either scattering or absorption is neglected and the wavelength dependency of the dust cross section is strongly simplified, e.g. by a gray body approximation. Nature, however, is usually not well approximated by such assumptions and numerical modeling is the only way to solve this problem.

Dust is detected in the majority of active galactic nuclei (Haas et al. 2008). According to the unified scheme (Antonucci & Miller 1985), AGN are surrounded by a dust obscuring torus. This torus, as argued by Krolik & Begelman (1988), needs a clumpy structure to allow the survival of dust grains in regions where the gas temperatures ($\sim 10^6$ K) are extreme compared to the dust sublimation temperature. Indeed, Tristram et al. (2007) show with VLTI observations of the Circinus active galactic nuclei (AGN) strong evidence for a clumpy or filamentary structure of the nucleus.

Electronic address: fheymann@pa.uky.edu

In this paper a numerical method is presented, which solves the radiative transfer equation in a three dimensional geometry, based on the Monte Carlo technique (Witt 1977; Sect.2). To reduce the required computational effort, different optimization strategies are developed (Lucy 1999; Bjorkman & Wood 2001; Gordon et al. 2001; Misselt et al. 2001; **?**; Baes 2008; Bianchi 2008; Baes et al. 2011; Sect. 3). Our numerical solution of the radiative transfer equation takes advantage of some of these optimization algorithms and is specifically developed to be vectorized and to run on graphics processing units (GPU). They are introduced into the original code developed by Krügel (2008). The MC routine handles arbitrary dust distributions in a three dimensional Cartesian model space at various optical depths. The self-consistent solution provides the dust temperatures; spectral energy distributions (SED) and images are computed using a ray–tracer (Sect. 4. The code is tested against existing benchmark results (Sect. 5). The influence of clumpiness of an AGN dust torus on the SED and the 10μm silicate feature is discussed and a model of the radio loud quasar 3C249.1 is presented (Sect. 6).

2. MONTE CARLO RADIATIVE TRANSFER

In our MC procedure the bolometric luminosity $L = \int_0^\infty L_\nu d\nu$ of the central engine is divided into $N = m\, n_{\rm zyk}$ monochromatic photon packets of equal energy $\xi = L/N$, where m is the total number of frequency

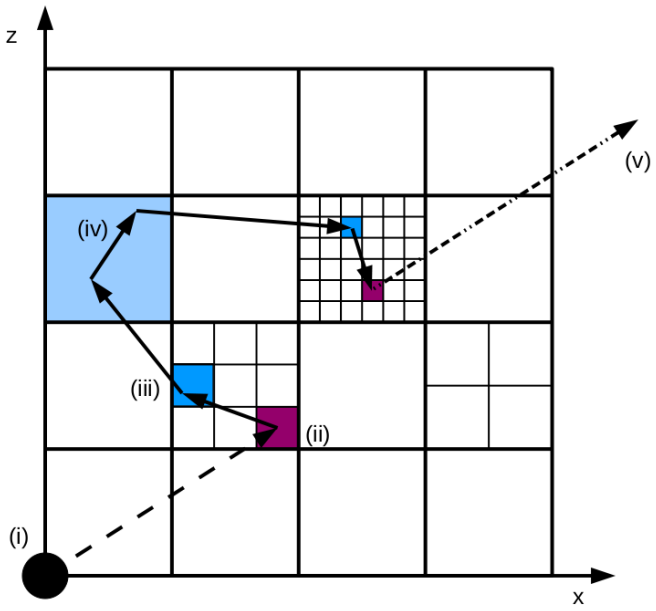

FIG. 1.— 2D illustration of the three dimensional grid and the trajectories of the photon packets. The grid is divided into cubes, which can be further divided into sub-cubes. The source emits photons at (i), which interact or not with the dust. By interaction photon packets are either absorbed (ii) or scattered (iii). Multiple interactions may occur in one cell (iv). After absorption the packet will be re-emitted by the dust at a different frequency. Frequency changes are illustrated by different line styles. Finally, (v) the packet escapes the model space.

bins of the heating source and $n_{\rm zyk}$ counts the number of photon packets per bin. The width of the frequency bin with index j between the frequencies ν_j and ν_{j+1}, $\Delta\nu = |\nu_{j+1} - \nu_j|$, is derived from the spectral shape of the radiation source and the energy of a photon packet

$$\xi = \int_{\nu_j}^{\nu_{j+1}} L_\nu d\nu \ . \tag{1}$$

The primary heating source emits photons for example in the optical and UV while the dust emission occurs at IR and sub-millimeter wavelength. Two frequency grids are considered: The first one is set up by Eq. (1) and accounts for the emission of the primary heating source. The second frequency grid is an extended version of the first one and includes additional bins in the IR and sub-millimeter to scope with the dust emission. The interaction probability between photons and dust particles in the radiative transfer problem is computed by the absorption κ_ν^{abs} and scattering κ_ν^{sca} cross-sections. The code includes different grain materials and size distributions.

The model space is set up as cubes in an orthogonal Cartesian grid. Each cube is divided into an arbitrary number of sub-cubes of volume V_i and constant density ρ_i (Fig. 1), where the index refers to subcube i. The subdivision of cubes allows a finer sampling whenever required: For example close to the dust evaporation zone, in regions of high optical depth or where the spatial gradient of the radiation field is large. One possible trajectory of a photon is illustrated in Fig. 1. Photons are emitted by the source at frequency $\nu_{j_\star}$, where $j_\star$ is the index of the frequency grid of the source. The flight path of the photon through out the model space is computed.

The direction of the photon is chosen from a uniform distribution of random numbers ζ_1, ζ_2 in the interval $[0, 1[$, so that $\phi = 2\pi\zeta_1$ and $\cos\theta = 1 - 2\zeta_2$. The distance from the entry point of a photon into a cell i to its exit point along the travel direction is ℓ_i. In the MC method the interaction of photons with the dust in a sub-cube can be determined with an uniform distributed random number ζ (Witt 1977; Lucy 1999) and the optical depth

$$\tau_i(\nu) = (\kappa_\nu^{abs} + \kappa_\nu^{sca})\ \rho_i\ \ell_i \ . \tag{2}$$

Photons leave the cell if $\tau_i \leq -\log\zeta$ and otherwise they interact with the dust. If a packet run through a cell without interaction it enters according to its travel direction a neighboring cell. At the border of the model space it eventually escapes. When a photon packet enters a cell a new random number is chosen to determine the interaction probability of photons with the dust [1]. The photon packet interacts with the dust after it has traveled a distance

$$\ell_i' = \frac{-\log\zeta}{\rho(\kappa_\nu^{abs} + \kappa_\nu^{sca})} \ . \tag{3}$$

The travel distance ℓ_i' defines the point in the cell where interaction takes place and photons are either scattered (Fig. 1.ii) or absorbed (Fig. 1.iii). Depending on its optical depth multiple scattering or absorption events may occur in a cell (Fig. 1.iv). In case of an interaction event the probability of scattering is given by the albedo $A_\nu = \kappa_\nu^{sca} \ / \ (\kappa_\nu^{sca} + \kappa_\nu^{abs})$ and therefore the chance of absorption is $1 - A_\nu$.

When a photon is scattered on a dust grain the packet keeps its frequency, but changes its travel direction according to the phase function of the particle. With the asymmetry factor g_ν, which approximates anisotropic scattering, the cross–section becomes $\kappa_\nu'^{sca} = (1 - g_\nu)\kappa_\nu^{sca}$. In the isotropic case the asymmetry factor g_ν equals 0. The index of the cell and the frequency of the scattered photon is stored. This allows us to compute the source function of the cell i, which will be used in a ray–tracer developed to compute the observed image at any frequency (Sect. 4).

When a photon is absorbed a new one with different frequency and direction is emitted from that position. The frequency of the emitted photon packet is given by the temperature of the absorbing material. The emitted photon has the same energy as the absorbed one. All photon packets contain the same amount of energy ξ, therefore the total number of absorbed photon packets per particle and cell is used to calculate the temperature of each material. After k absorptions of photon packets by dust the cell i has a temperature $T_{i,k}$ calculated from:

$$\int \kappa_\nu^{abs} B_\nu(T_{i,k})\ d\nu \ = \ \frac{k\xi}{4\pi\rho_i V_i} \ , \tag{4}$$

where $B_\nu(T_{i,k})$ is the Planck function.

Dust emits a photon packet at the shortest frequency ν' calculated with:

[1] It can be confirmed that the interaction probability calculated with a new random number is in agreement with the treatment of a travel distance which is determined by a single random number (Lucy (1999)).

$$\int_0^{\nu'} \kappa_\nu^{abs}\ B_\nu(T_{i,k})\ d\nu\ \geq\ \zeta \int_0^{\infty} \kappa_\nu^{abs}\ B_\nu(T_{i,k})\ d\nu\ . \quad (5)$$

In the Monte Carlo method one follows all N photon packets through the dust cloud until they reach the outer boundary of the model and escape. For each cell the absorption events are counted. When all packets escaped the model space, the number of absorptions in a cell is used (Eq. (4)) to calculate its dust temperature. An iterative MC method is started with an initial guess of the dust temperatures. This allows to compute the frequencies of packets emitted by the dust (Eq. (5)). After all packets escaped the model space another N photons are emitted by the source and their flight paths through the model are computed. However, this time using the dust temperatures of the previous run. This procedure continues until the dust temperatures converges, which usually takes about 3–5 iterations.

3. OPTIMIZED MONTE CARLO RADIATIVE TRANSFER

In this section we describe various optimization techniques which are introduced into our MC scheme to increase the accuracy and decrease computing times.

3.1. *Small optical depth*

The Monte Carlo approach solves the radiative transfer problem in a probabilistic way. Dust temperatures become uncertain and have large errors whenever the interaction probability is low. This is the case in cells of low optical depth where many photons fly–by without being absorbed or scattered by the dust. The statistical noise in such cells can be reduced significantly applying a procedure developed by Lucy (1999). Contrary to the method described in Sect. 2, in which only absorption events contribute to the temperature calculation of the cell, the Lucy method considers the absorbed energy of every photon packet traveling through the cell. This technique increases the temperature accuracy of the MC treatment in low optical depth regions. It has no advantage when the optical depth $\tau_i \geq 1$ as interactions between photons and dust are likely.

We follow Sect.3.4 of Lucy (1999) and implement a similar optimization technique. Whenever the maximal optical depth of a cell i is smaller than 10^{-2}, the energy absorbed by the dust $E_i^{\rm abs}$ is a small fraction of the energy of a photon packet and it holds that

$$E_{\rm i}^{\rm abs} = (1 - e^{-\tau_{\rm i}})\,\xi \quad (6)$$

where $\tau_{\rm i}$ is the optical depth from the entry to the exit point of the photon of cell i. Thereby the frequency of the photon packet remains unchanged.

3.2. *High optical depth*

The Monte Carlo solution of the radiative transfer equation becomes slow for very optical thick regions, where the number of photon interactions with the dust increases exponentially. To avoid photons getting trapped in cells of very high optical depth a modified random walk procedure which is based on the diffusion approximation is presented by Fleck Jr. & Canfield (1984). The method is tested by Min et al. (2009) and numerical enhancements are given by Robitaille (2010).

3.3. *Iteration–free Monte Carlo*

An iteration free Monte Carlo scheme is developed by Bjorkman & Wood (2001) (B&W); see Baes et al. (2005); Krügel (2008) for helpful comments. In the B&W method the temperature of the dust in a cell is immediately adjusted so that the frequency ν' of the emitted photon is corrected to the previous events. Contrary to Eq. (5), dust re-emission occurs at the shortest frequency ν' for which

$$\int_0^{\nu'} \kappa_\nu^{abs} \frac{dB_\nu(T_k)}{dT} d\nu\ \geq\ \zeta \int_0^{\infty} \kappa_\nu^{abs} \frac{dB_\nu(T_k)}{dT}\ d\nu \quad (7)$$

is valid. Both methods described in Eq. (5) and Eq. (7) are implemented in the MC code and can be used upon preference.

3.4. *Parallelization on graphics processing units*

The Monte Carlo method to solve the radiative transfer problem is particularly suited for parallelization because all photon packets are independent of each others (Jonsson 2006; Heymann 2010; Siebenmorgen et al. 2011). By vectorization of the code a number of photon packets are emitted simultaneously. The number of packets launched at a time depends on the threads[2] available on the computer. The trajectories of the photons can then be calculated in parallel. In parallel environments an additional requirement is set on the random number generator. Sequences of random numbers must be independent per thread. We solve this problem by applying a parallel version of the Mersenne Twister algorithm as given by Matsumoto & Nishimura (2000).

Parallelization is most efficient when all processing units finish their task within the same amount of time. Then vectorization speeds up the code roughly equal to the number of threads available. Unfortunately this is not always the case. The number of interactions of photons increases exponentially with the optical depth $\tau_{\rm V}$ and photon packets may get trapped in cells with say $\tau_{\rm V} \geq 1000$. The workload of these cells is much higher than for cells at much lower optical depth. This results in a rather unbalanced workload over all threads so that the advantage of vectorization slows down considerably or may even get lost. In our application idle threads are avoided as much as possible. Every-time a thread finishes the trajectory of the photon packet within the model space a counter is increased. If the counter reaches 80% of the total number of parallel working threads and if the number of interactions of the photon packet within a cell is larger than 100 the thread pauses. In this case the position and frequency of the photon packet is stored. Close to the end of the simulation when all photons with average processing speed escaped the model space, the stored photons are resumed. This procedure allows a balanced workload among all threads. In addition the modified random walk procedure of Robitaille (2010) is implemented (Sect. 3.2.)

This code utilizes two different parallelization methods. It can be used on shared memory machines using the openMP library to run as many parallel rays as there

[2] A thread is the smallest unit of processing that can be scheduled in a parallel environment.

TABLE 1
Run time requirements of different Monte Carlo methods.

Method	Threads	Time (min.)
Lucy	1	180
B&W	1	60
Lucy	8	45
B&W	8	20
GPU	256	3
GPU+Lucy	256	4
GPU+B&W	256	2
GPU+B&W+Lucy	256	2

are processor cores available and on vectorized hardware (GPU) highly optimized for parallelization. The complete Monte Carlo radiative transfer solution is ported to GPU using the Compute Unified Device Architecture (CUDA) developed by NVIDIA (CUDA 2011). This speeds up the entire MC solution in comparison to the method by Jonsson & Primack (2010), which provides only a GPU acceleration when computing the temperature of a grain.

3.5. *Parallelization and optimization algorithms*

The run time requirements of the different Monte Carlo methods are compared. We consider a star at temperature of 2500 K with solar luminosity which heats a spherical and constant density dust envelope with an inner radius of 0.7 AU and an outer radius of 700 AU. The optical depth is measured from the star to the outer boundary is $\tau_V = 10$. Parameters of the dust are specified as in Sect. 5.1. In the models 10^7 photon packets are emitted from the star and 10^6 grid cells are used.

We apply the Lucy (Sect.3.1), B&W (Sect.3.3.) method in a scalar (single thread), a CPU version with 8 threads, a GPU version with 256 threads and in addition the iterative MC scheme of 2 on a GPU machine. Initializing times of the various MC methods are identical.

As described in Sect.3.1 for the same number of emitted photon packets the Lucy method provides a better temperature estimate than the other methods. In the Lucy method the fraction of a photon packet is considered. This can only be realized by considering floating point operations which are more computer expensive than integer operations. In our test case the scalar version of the Lucy method is run with three iterations and requires a total run time of 3 hours (Tab. 1).

For single thread applications the iteration–free MC scheme by B&W (Sect. 3.3) has the advantages that it speeds up the process by a factor which equals the number of iterations required for convergence in the other MC treatments. However, in the B&W method memory interaction between different cells are unavoidable and they slow down the parallelization capabilities of this method. The memory interaction between cells rises with the number of threads and therefore the amount of necessary *atomic memory operations*[3] increases with parallelization. To minimize the number of atomic memory operations we solve the problem in an iterative MC scheme using Eq. (4). This allows parallelization with a huge number of threads. At low budget this can be realized using GPU technology and these MC methods are labeled as such in column 1 of Table 1. The GPU method may be further optimized in combination with the Lucy (GPU+Lucy) or the B&W method (GPU+B&W). On our conventional computer we use a GPU with 256 threads (8 multiprocessor each with 32 cores) clocked at 1.5 GHz. When compared to a single thread CPU application clocked at 3 GHz a speed up factor due to vectorization of 60 is realized. This is below a theoretical expected speed up factor of 128 because of additional overheads produced by input/output routines and memory transfers in the GPU machine.

Total run times of the various methods with different numbers of threads are given in Table 1. The vectorized Lucy method scales slightly better with the number of available threads than the other algorithms because fewer atomic memory operations are required. The speed increase by vectorization as compared to scalar MC treatments is proportional to the number of available threads. The GPU method with B&W optimization becomes a factor 90 faster than the original Lucy method.

[3] Atomic operations are operations which are performed without interference from any other threads. Atomic operations are often used to prevent conditions which are common problems in multi–thread applications.

4. RAY–TRACER TO COMPUTE SEDS AND IMAGES

Photons which eventually escape the MC model space in a particular solid angle can be counted and converted into a flux density. In principle this method allows to compute images of the object. Unfortunately to obtain a moderate signal–to–noise ratio the number of photon counts per solid angle must be high which is difficult to reach within reasonable computing times. Here we present a ray–tracing method which allows us to compute noise free images, SEDs and visibilities at high spatial resolution. The ray–tracer uses the temperature and scattering events of the cells calculated with the MC code (Sect. 2). The uncertainty in the derived images is therefore based on the precision of the MC computation.

In the algorithm rays are traced from an arbitrary oriented observer plane through the model space of the MC cube. The ray tracer together with the MC method allows us to calculate the flux received on each pixel of an image in the plane of the observer. The observed image is located at distance D from the object which is the center of the cube. The orientation of the image plane is defined by its surface normal $\vec{e}_z{}'$. The axis of the image plane $\vec{e}_x{}'$, $\vec{e}_y{}'$ is perpendicular to $\vec{e}_z{}'$. The coordinates (x, y, z) of the 3D model space are transformed by a parallel projection into the coordinates (x', y') of the 2D image in the observers plane. The image consists of $n_x \times n_y$ pixels, with a pixel size chosen so that the complete model fits in the projection. The center of the image $\vec{i}_0$ is located at position $[x_0, y_0, z_0]$ and has image coordinates $[x'_0, y'_0]$. The projected coordinates $[x', y']$ of the image are transformed into MC cube coordinates by

$$\vec{r}(x', y') = \vec{i}_0 + (x' - x'_0)\ \vec{e}_x{}' + (y' - y'_0)\ \vec{e}_y{}' \ , \quad (8)$$

where $\vec{r} = [x, y, z]$. The ray–tracer follows the line of sight from each detector pixel in direction $\vec{e}_z{}'$ through the MC model. Adding the contribution of emission and scattering from each cell i along the line of sight results

in the observed intensity. The contribution of cell i to the total intensity is

$$I_{\nu,i} = (I^e_{\nu,i} + I^s_{\nu,i})\ e^{-\tau_{\nu,i}}\ , \tag{9}$$

where $I^e_{\nu,i}$ refers to the intensity of the dust emission and $I^s_{\nu,i}$ to scattering; $\tau_{\nu,i}$ is the optical depth at frequency ν of cell i. For convenience we drop in the following index i, the optical depth is

$$\tau_\nu = \mathrm{K}^{abs}_\nu \int_0^\ell \rho\,(\vec{r})\,ds\ , \tag{10}$$

where K^{abs}_ν is the absorption cross section per unit dust mass and ℓ is the path lengths. It is measured along the ray from the border of the MC model to a point in cell i which is at half–distance between both piercing points of that cell. The dust mass of cell i is $\rho_i\ V_i$. The emission is

$$I^e_\nu = \rho_i\ V_i\ \mathrm{K}_\nu{}^{abs}\ \mathrm{B}_\nu(T)\ . \tag{11}$$

For isotropic scattering the intensity is given by the total number of scattering events N^{sca}

$$I^s = \frac{N^{sca}\epsilon}{4\pi\ \Delta\nu}\ , \tag{12}$$

where $\Delta\nu$ is the width of the frequency bin. The flux density is computed summing up the contribution of each cell given by

$$F_{\nu,\mathrm{i}} = \frac{1}{D^2}\big[\rho_i\ V_i\ \mathrm{K}^{abs}_\nu \mathrm{B}_\nu(T_\mathrm{i}) + \frac{N^{sca}_{\nu,i}\epsilon}{4\pi\Delta\nu}\big]\ e^{-\tau_\nu}\ . \tag{13}$$

5. BENCHMARK

The vectorized MC method is tested against the 1d ray tracing code by Krügel (2008). Further verifications of the MC and comparison with benchmark tests are described below

5.1. *Spherical symmetry (1D)*

Benchmark models in 1D are provided by Ivezic et al. (1997). They consider a spherical dust envelope which is centrally heated by a 2500 K star with luminosity of $1 L_\odot$. For the test the dust absorption and scattering coefficient are for wavelength below $\lambda_0 = 1\mu$m: $q_\mathrm{abs} = q_\mathrm{sca} = 1$ and for longer wavelengths: $q_\mathrm{sca} = \lambda_0/\lambda$ and $q_\mathrm{abs} = (\lambda_0/\lambda)^{-4}$. Models are computed at optical depths of $\tau_\mathrm{V} = 1$, 10, 100 and 1000 with inner radius $r_\mathrm{in} = 3.14$, 3.15, 3.20 and 3.52 AU, respectively. The dust density is constant and the outer radius is $r_\mathrm{out} = 1000 \times r_\mathrm{in}$. The models are run on a grid with 10^6 cells and 2×10^8 photon packets per iteration are launched from the star. The number of MC iterations are 3, 4 and 5 for $\tau_\mathrm{V} \le 10$, 100 and 1000, respectively.

MC computed temperatures are compared to the one calculated by DUSTY (Ivezic & Elitzur 1997) and Krügel (2008); they agree within $\lesssim$1 %. The SEDs are shown in Fig. 2 in which each quadrant represents models at different optical depths. In the quadrants the SED are shown in the top and the flux difference between MC and benchmark in the bottom panel. The SED of the MC models are either computed by photon counting or using the ray–tracer (Sect. 4). The difference of the SED computed by MC and DUSTY is typically better than a few %. It becomes larger at faint fluxes where the ray tracing is more accurate than the packet counting procedure because of photon noise. For the $\tau_\mathrm{V} = 1000$ model the counting method starves at fluxes below 0.2% from the peak flux. We encountered numerical inconsistencies in the DUSTY code at flux levels $\lesssim 10^{-8}$ from the peak when compared against the radiative transfer code by Krügel (2008).

5.2. *Disk geometry (2D)*

TABLE 2
PARAMETERS OF 2D BENCHMARK BY PASCUCCI ET AL. (2004)

Symbol	Parameter	Value
$\mathrm{M}_\star$	Stellar Mass	1 $\mathrm{M}_\odot$
$\mathrm{R}_\star$	Stellar Radius	1 $\mathrm{R}_\odot$
$\mathrm{T}_\star$	Stellar effective temperature	5800K
r_in	Inner disk radius	1 AU
r_out	Outer disk radius	1000 AU
r_d	Half of outer radius	500 AU
z_d	Disk height	125 AU
a	Grain radius	0.12 μm
ρ_0	Density for $\tau_\mathrm{V} = 1$	$8.45\,10^{-22}\mathrm{gcm}^{-3}$
τ_v	Optical depth at 550 nm	$1, 10, 100$

Different methods to compute the RT in a 2D dust configuration are compared by Pascucci et al. (2004). They consider a star which heats a dust disk. The inner region $r < r_\mathrm{in}$ is dust free and the dust density distribution is similar to those described by Chiang & Goldreich (1997, 1999):

$$\rho(r,z) = \rho_0\ (\frac{r_d}{r})\ e^{-(0.25\pi(z/h)^2)} \tag{14}$$

with

$$h = z_d\ (\frac{r}{r_d})^{1.125}\ , \tag{15}$$

where r is the distance from the central star in the mid-plane of the disc and z is the height above the mid-plane. The parameter ρ_0 is chosen such that the optical depth at 550 nm along the mid-plane is 1, 10 and 100, which leads to densities $\rho_0 = 8.45\,10^{-22}, 8.45\,10^{-21}$ and $8.45\,10^{-20}$ g cm^{-3}. Additional parameters are specified in Table 2. The absorption and scattering cross sections are that of a 0.12μm silicate grain (optical data[4] are taken from **?**).

The SEDs calculated by the various algorithms and treatments used by Pascucci et al. (2004) agree to better than 20%. The RT in the disk is solved by our GPU code and the derived SED are compared to an averaged SED of the results given by Pascucci et al. (2004)

In the Monte Carlo program we use 3×10^6 cells and run models with 2×10^8 photon packets per iteration.

For the optical depth along the mid-plane of the disk with $\tau_\mathrm{V} \le 10$ we use 3 iterations and found in the SED an overall agreement to the benchmark results to within a few %. In the $\tau_\mathrm{V} = 100$ case 4 iterations are used and the SED and differences to a mean SED over those computed in the reference models is shown in Fig. 3.

[4] download from
http://www.mpia.de/PSF/PSFpages/RT/benchmark.html

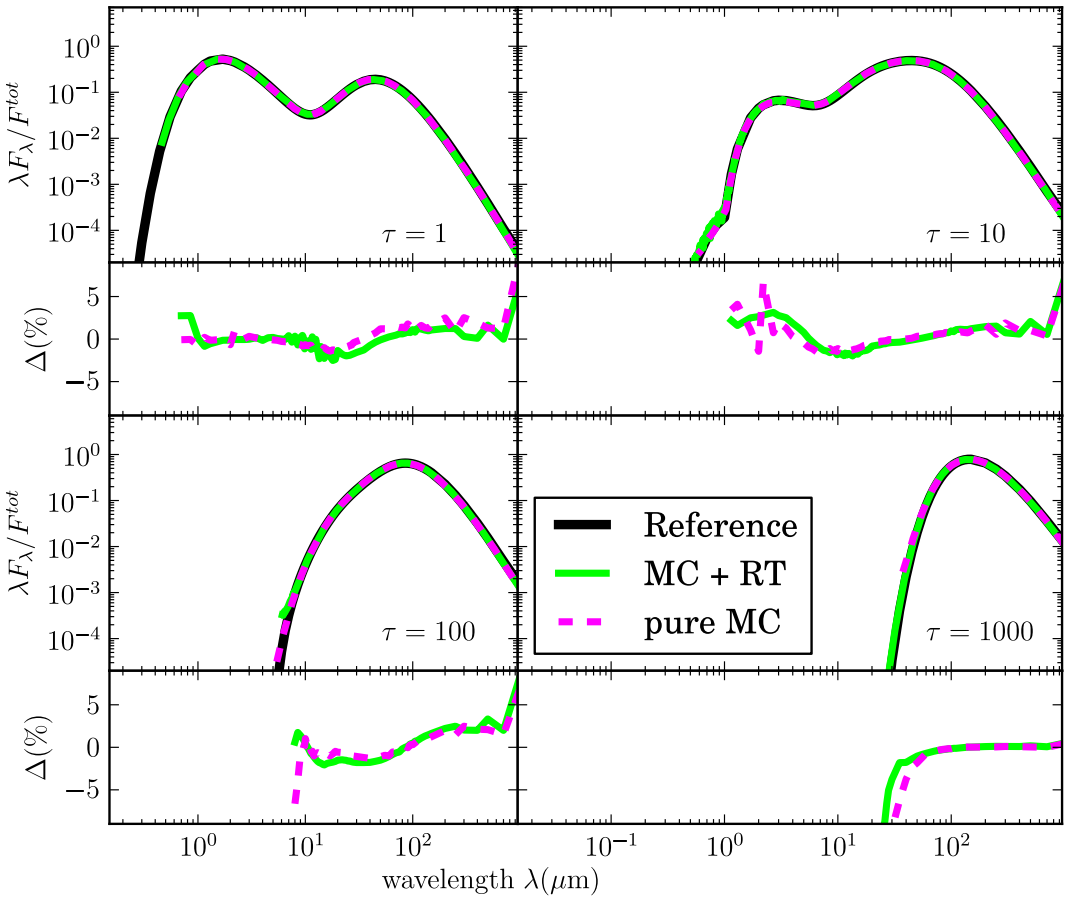

FIG. 2.— Comparison of SEDs of dust spheres at optical depths between $\tau_V = 1$ and 1000 computed with MC and ray–tracer (green) or photon counting (dashed), benchmark results in black (Ivezic et al. (1997)). Lower panels give the difference between benchmark and the procedures of this work.

Two different inclinations 12.5° (face–on), 77.5° (edge–on) are displayed. The residual between SED computed by us and the mean SED of the benchmarks is typically a few % and larger deviation are found at fluxes below 1% of the peak flux. This is visible at the border of the wavelength grid and in the 10μm silicate absorption band where variations from one SED to another in the reference codes are also larger.

6. CLUMPY AGN TORUS MODEL

The unified scheme of AGN (Antonucci & Miller 1985; Padovani & Urry 1990) predict that the central engine is surrounded by dust so that the obscuration depends on the viewing angle. The detailed geometrical configuration of dust around the AGN is still a matter of debate (Stalevski et al. 2011). Observations are not able to resolve the inner part of the objects. Theoretical considerations favor a toroidal and clumpy geometry (Nenkova et al. 2002; Schartmann et al. 2005; Hönig et al. 2006; Nenkova et al. 2008; Schartmann et al. 2008, 2010). Observational hints of a clumpy structure in which optical thick dust clouds surround the accretion disc of the central black hole are provided by the 10μm silicate band. This band is detected in absorption and emission. The strength of the feature is much weaker than predicted by homogeneous torus models (Pier & Krolik 1992; Granato & Danese 1994; Efstathiou & Rowan-Robinson 1995; van Bemmel & Dullemond 2003). A silicate emission feature is also seen in obscured AGN, where the broad emission lines are hidden (Sturm et al. 2006; Mason et al. 2009). Observations are explained by postulating a clumpy torus structure.

For the dust around AGN we consider fluffy agglomerates of silicate and carbon as sub-particles. We use a power law size distribution: $n(a) \propto a^{-3.5}$ with particle radii between $a_- \leq a \leq a_+$ and $a_- = 160$Å, $a_+ = 0.13\mu$m. The bulk density of both materials is $2.5\,\mathrm{g/cm^3}$. Dust abundances (ppm) are 31 [Si]/[H] and 200 [C]/[H], which agree with cosmic abundance constrains (**?**). This gives a gas–to–dust mass ratio of 130. As relative volume fraction of the composite grain we use 34% silicates, 16% carbon and 50% vacuum, which translates, with abundances as above, to a relative mass fraction of 68% silicates and 32% amorphous carbon. Absorption and scattering cross-sections and the scattering asymmetry factor is computed with Mie theory and the Bruggeman mixing rule. Optical constants are for silicates by Draine (2003) and carbon by **?**. This gives a total mass extinction cross section in the optical (0.55μm)

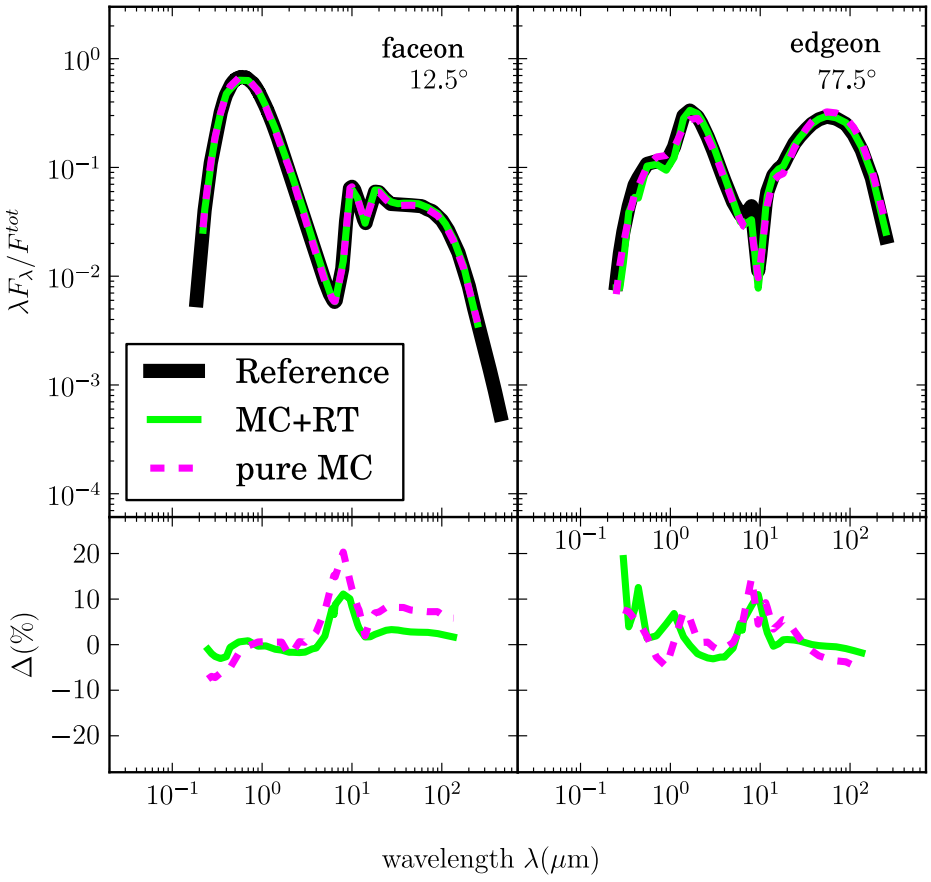

FIG. 3.— Comparison of SEDs of a dust disk at optical depths along the mid-plane of $\tau_V = 100$, face-on view (12.5°) is shown left and edge-on view (77.5°) right. SEDs are computed with MC and ray–tracer (green) or photon counting (dashed). The mean SED of the benchmark results by Pascucci et al. (2004) is in black. Lower panels give the difference between the mean SED of the benchmark and the procedures of this work.

of $K_V^{ext} = 35000$. The wavelength dependence of K^{ext} is displayed in **?**.

The hard (UV/optical) AGN radiation emerges from the accretion disc around the massive black hole. Its spectral shape is suggested to follow a broken power law (Rowan-Robinson 1995):

$$\lambda F_\lambda \propto \begin{cases} \lambda^{1.2} & \text{for} \quad -\infty < \lambda < 0.01\mu\text{m} \\ \text{const} & \text{for} \quad 0.01 < \lambda < 0.10\mu\text{m} \\ \lambda^{-0.5} & \text{for} \quad 0.1 < \lambda < 1.0\mu\text{m} \\ \lambda^{-3} & \text{for} \quad 1.0 < \lambda < +\infty \end{cases} \tag{16}$$

In the following we consider a clumpy AGN dust torus of total luminosity of $L_{45} = 10^{45}$ erg/s. The inner radius of the torus $r_{\rm in}$ is set by dust evaporation, which is approximated by $r_{\rm in} = 0.4\ (L_{45})^{0.5}$ pc. A clump is represented as a sphere of constant density and radius of 0.5 pc. The optical depth through the center of the clump is $\tau_V = 30$. The clumps are randomly distributed within a half opening angle of $\theta = 45°$ within the inner radius of $r_{\rm in} = 0.3$ pc and the outer radius of $r_{\rm out} = 6$ pc. For random numbers $\zeta_1, \zeta_2, \zeta_3$ the position of the center of the clouds is computed by

$$\begin{aligned} r &= \zeta_1\ (r_{\rm out} - r_{\rm in}) \\ \phi &= 2\pi\ \zeta_2 \\ \theta &= \frac{\pi}{2} + (2\ \zeta_3 - 1)\theta_1\ . \end{aligned} \tag{17}$$

If clumps overlap the density is constant and the same as for a single clump.

6.1. *Influence on clumps on SED*

The AGN torus model is used to study the influence of clumps on the SED. In the models the number of clouds is varied using $N_{\rm clump} = 500, 1000$ and 2000. This gives a total optical depth along the mid-plane of the torus of $\tau_V \sim 80$, 140 and 200. The SED is displayed in Fig. 4; at wavelengths $\lesssim 1\,\mu$m, the flux is emitted by the central source and between 1μm and 50μm the SED is dominated by dust emission. The dust temperatures are between 100 and 1500 K. At short wavelengths of the SED the AGN is visible only in the face–on view and becomes faint at higher inclination angles. At longer wavelengths the flux is stronger in the edge–on view as compared to observations at smaller inclination angles. The optical depth of a single clump is high and already one or two

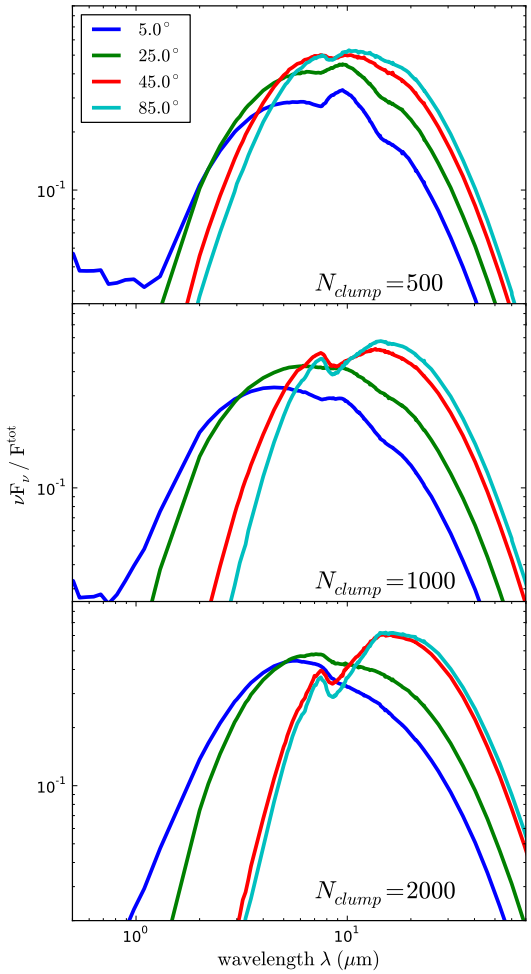

FIG. 4.— Spectral energy distribution of clumpy AGN torus models at viewing angles between 5° and 85° and number of clouds of $N_{\rm clump}$ = 500, 1000 and 2000.

of such intervening clouds define most of the spectral behavior of the torus. The SEDs at viewing angles between 45° and 85° are similar. At these angles always a few clouds are in the line of sight and dominate the spectrum (Fig. 4).

Depending on the total optical depth and temperatures of the dust the 10 μm silicate band of AGN are observed in emission or absorption. In AGN viewed face–on (type I sources) there is a direct view on the inner region of the torus and a weak 10μm silicate emission feature is observed (Siebenmorgen et al. 2005; Hao et al. 2005; Sturm et al. 2005). In edge–on sources (type II) the 10μm silicate band is seen in absorption.

The silicate features trace the amount of dust for a given viewing direction and constrains the distribution of the clumps in the torus (Nikutta et al. 2009). Homogeneous AGN torus models without a clumpy structure over predict the strength of the silicate feature (Efstathiou & Rowan-Robinson 1995). In the clumpy torus models presented in Fig. 4 the 10μm feature is in emission for face-on views as long as $N_{\rm clump} \lesssim 1000$. Individual clouds are optical thick at 10μm so that a single cloud already obscures the warm and optical thin region required to observe the silicate band in emission. This is the case in the face-on view of the model with 2000 clumps where the emission and self–absorption of the silicate grains cancels out and the spectrum becomes featureless. For inclination angles $\theta \geq 45°$ the silicate features is in absorption (**?**). The strength of the absorption feature depends on the optical depth and therefore increases with increasing number of clumps.

6.2. *AGN images*

The MC combined with the ray–tracer (Sect. 4) allows us to compute images of the object at a given wavelength. In Fig. 5 we present a 10μm and 0.55μm image of the clumpy AGN torus using $N_{\rm clump}$ = 1000. The mid IR image is dominated by dust emission and the optical image by scattered light. The face-on image in the mid IR provides an unobscured view of the emission from hot dust in the inner torus close to the AGN. In the image clouds near the center dominate the emission. Further out, clumps become cooler and the contribution to the emission decreases. In the tilted view, at 45°, intervening clumps obscure part of the emission from the central region and the contribution of cooler dust becomes more important than in the face–on view. In the edge-on view most of the central region is no longer visible and the emission is dominated by clouds located close to the border of the torus. However, because of the clumpy nature of the medium close to the edge–on view there are still a few lines of sight penetrating to the inner torus. This is not the case in AGN models using a homogeneous dust distribution. For all viewing angles and clump configurations the scattered light images appear similar to the emission images (Fig. 5). However, the flux in the optical is two orders of magnitude fainter than at 10μm. The scattering light image in the edge-on view becomes fuzzy.

6.3. *Quasar 3C 249.1*

The clumpy AGN dust torus model is applied to fit the SED of the quasar 3C249.1. The luminosity of the object is 7×10^{45} erg/s at redshift of $z = 0.311$ which translates, using standard cosmological parameters, to a luminosity distance of 1600 Mpc. The torus inner edge is set by the sublimation temperature and leads to an inner radius of $r_{\rm in} = 1$ pc. In the inner region of the model at $r \leq 25 \times r_{\rm in}$ the half opening angle of the torus is $\theta_1 = 25°$ and in the outer region up to $r_{\rm out} = 50 \times r_{\rm in}$ it is 55°. The torus includes 5500 clouds. The number of clumps per volume element decreases in the inner part and increases in the outer part of the torus; other parameters remain the same.

In order to fit data at $\lambda > 40\mu$m we increased the outer radius of the torus $r_{\rm out}$ and considered a two phase medium in which the density in between the clumps is varied. However, the far IR emission of the quasar cannot be explained by the AGN torus. The far IR is dominated by emission of cold dust located further-out in the host galaxy. For simplicity we approximate this cirrus component by a modified black body, $\kappa_\nu^{abs} B_\nu(T)$ at 50 K. The dust torus model fit the silicate emission feature as observed in the Spitzer spectrum and together with the cirrus component a good fit to the overall SED is achieved (Fig. 6).

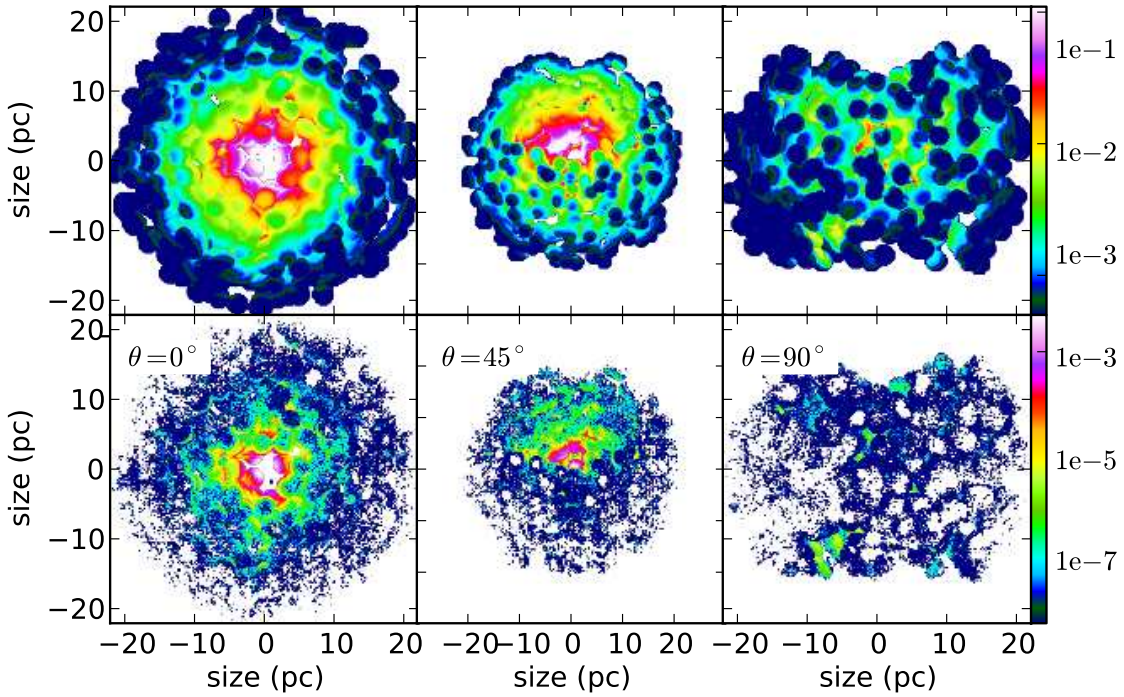

FIG. 5.— Images at 10μm (top) and 0.55μm (bottom) of the clumpy AGN torus with $N_{\rm clump} = 1000$ and viewing angles (from left to right) of 0°, 45° and 90°. . Color bar gives flux in (Jy/arcsec^2). The source with luminosity L=10^{45} erg/s is at a distance of 15 Mpc

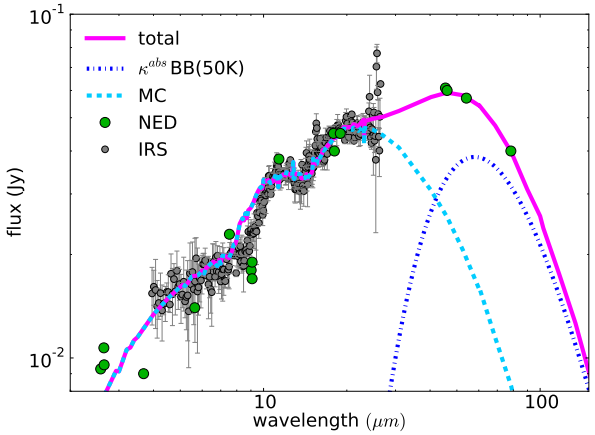

FIG. 6.— IR emission of the quasar 3C249.1. Photometric data by NED and Spitzer spectrum by Siebenmorgen et al. (2005). The total flux (full line) is given as sum of the clumpy AGN torus model (dashed) and a cirrus component (dashed dotted).

7. CONCLUSIONS

A parallel 3D Monte Carlo method is presented to solve the radiative transfer problem of dust obscured objects in arbitrary geometries. The code uses an adaptive three dimensional Cartesian grid. It utilizes the advantage of different optimization algorithms: in optical thin cells the Lucy algorithm and in cells at very high optical depths a modified random walk procedure by Fleck Jr. & Canfield (1984) is included. The temperature of the dust is computed in an iteration MC method or with the iteration–free Bjorkman & Wood (2001) algorithm.

The spectral energy distribution of the objects is derived by a photon counting procedure or a ray–tracing routine. Photons which eventually escape the MC model space are counted and converted into a flux density. This method computes the SED of an object very fast when a large aperture of several degree is used. Unfortunately, for high spatial resolution the method starves with the count rate. The SED of an object observed with a pencil beam is computed by a ray tracer which uses the dust scattering and absorption events of the MC cells as input. The ray tracer allows to compute noise free images of the scattered and emitted radiation at any frequency.

Monte Carlo schemes are known to be computing time expensive. Therefore we put particular attention to solve this problem. We use the advantage that the trajectories of the MC emitted photon packets can be traced independent of each others. This allows a highly vectorized design of the MC program which is not realized

in previous work. With the vectorized code a speed improvement of about 100 is reached on a low budget computer when compared to a scalar, non–parallel version of the same program. This gain in the speed performance of the computations is reached by applying either a multi–core application using conventional central processing units (CPU) or the recent technological development of graphics power units (GPU). The parallelization capabilities of various MC radiative transfer algorithms are analyzed. By combining different MC algorithms we report a linear scaling of the computing time with the number of available threads (processor cores). The ray-tracer to compute SED and images is another computer time expensive procedure and is developed, similar to the MC code, in vectorized form.

The 3D Monte Carlo is tested against the ray tracer solution of the radiative transfer problem in spherical symmetry by Krügel (2008). Further we verified our procedure against one and two dimensional benchmarks of the literature. The code reproduces the spectral energy and dust temperature distributions of the test cases at high accuracy. As a first astrophysical application we use the Monte Carlo code to investigate the appearance of a dusty AGN at optical and IR wavelengths; a second application on proto-planetary disks is presented in an accompanying paper (**?**)

The dust around the AGN is geometrically configured in a clumpy torus structure and is represented by fluffy composite grains of various sizes made of silicate and carbon. The influence of the number of clumps in the torus on the SED is studied. We find that the clumpy torus explains the observed "weak" silicate absorption and emission feature observed in AGN. Images of the AGN in the optical and the mid IR are presented by viewing the torus from different angles. The spectral energy distribution of the radio loud quasar 3C249.1 is fit by the torus model and a cirrus component for the far IR and sub-millimeter emission is included.

We are grateful to Endrik Krügel for discussions and helpful suggestions. This work is based in part on observations made with the *Spitzer Space Telescope*, which is operated by the Jet Propulsion Laboratory, California Institute of Technology under a contract with NASA.

REFERENCES

Andre, P. & Montmerle, T. 1994, ApJ, 420, 837
Antonucci, R. 1993, ARA&A, 31, 473
Antonucci, R. R. J. & Miller, J. S. 1985, ApJ, 297, 621
Baes, M. 2008, MNRAS, 391, 617
Baes, M., Stamatellos, D., Davies, J. I., et al. 2005, New Astronomy, 10, 523
Baes, M., Verstappen, J., De Looze, I., et al. 2011, ApJS, 196, 22
Bianchi, S. 2008, A&A, 490, 461
Bjorkman, J. E. & Wood, K. 2001, ApJ, 554, 615
Calzetti, D., Kinney, A. L., & Storchi-Bergmann, T. 1994, ApJ, 429, 582
Chiang, E. I. & Goldreich, P. 1997, ApJ, 490, 368
Chiang, E. I. & Goldreich, P. 1999, ApJ, 519, 279
CUDA. 2011, NVIDIA C Programming Guide
Draine, B. T. 2003, ARA&A, 41, 241
Dullemond, C. P. & Monnier, J. D. 2010, ARA&A, 48, 205
Efstathiou, A. & Rowan-Robinson, M. 1995, MNRAS, 273, 649
Fleck Jr., J. & Canfield, E. 1984, Journal of Computational Physics, 54, 508
Gordon, K. D., Misselt, K. A., Witt, A. N., & Clayton, G. C. 2001, ApJ, 551, 269
Granato, G. L. & Danese, L. 1994, MNRAS, 268, 235
Haas, M., Willner, S. P., Heymann, F., et al. 2008, ApJ, 688, 122
Hao, L., Spoon, H. W. W., Sloan, G. C., et al. 2005, ApJ, 625, L75
Heymann, F. 2010, PhD thesis, University of Bochum, "http://www-brs.ub.ruhr-uni-bochum.de/netahtml/HSS/Diss/HeymannFrank/diss.pdf"
Hönig, S. F., Beckert, T., Ohnaka, K., & Weigelt, G. 2006, A&A, 452, 459
Ivezic, Z. & Elitzur, M. 1997, MNRAS, 287, 799
Ivezic, Z., Groenewegen, M. A. T., Men'shchikov, A., & Szczerba, R. 1997, MNRAS, 291, 121
Jonsson, P. 2006, MNRAS, 372, 2
Jonsson, P. & Primack, J. R. 2010, arXiv, 15, 509
Krolik, J. H. & Begelman, M. C. 1988, ApJ, 329, 702
Krügel, E. 2008, An introduction to the physics of interstellar dust (Springer)
Lissauer, J. J. 1993, ARA&A, 31, 129
Lucy, L. B. 1999, A&A, 344, 282
Mason, R. E., Levenson, N. A., Shi, Y., et al. 2009, ApJ, 693, L136
Matsumoto, M. & Nishimura, T. 2000, in Monte Carlo and Quasi-Monte Carlo Methods 1998 (Springer), 59–69
Min, M., Dullemond, C. P., Dominik, C., de Koter, A., & Hovenier, J. W. 2009, A&A, 497, 155
Misselt, K. A., Gordon, K. D., Clayton, G. C., & Wolff, M. J. 2001, ApJ, 551, 277
Nenkova, M., Ivezić, Ž., & Elitzur, M. 2002, ApJ, 570, L9
Nenkova, M., Sirocky, M. M., Ivezić, Ž., & Elitzur, M. 2008, ApJ, 685, 147
Nikutta, R., Elitzur, M., & Lacy, M. 2009, ApJ, 707, 1550
Padovani, P. & Urry, C. M. 1990, ApJ, 356, 75
Pascucci, I., Wolf, S., Steinacker, J., et al. 2004, A&A, 417, 793
Pier, E. A. & Krolik, J. H. 1992, ApJ, 399, L23
Popescu, C. C. & Tuffs, R. J. 2005, in American Institute of Physics Conference Series, Vol. 761, The Spectral Energy Distributions of Gas-Rich Galaxies: Confronting Models with Data, ed. C. C. Popescu & R. J. Tuffs, 155–177
Robitaille, T. P. 2010, A&A, 520, A70+
Rowan-Robinson, M. 1995, MNRAS, 272, 737
Schartmann, M., Burkert, A., Krause, M., et al. 2010, MNRAS, 403, 1801
Schartmann, M., Meisenheimer, K., Camenzind, M., Wolf, S., & Henning, T. 2005, A&A, 437, 861
Schartmann, M., Meisenheimer, K., Camenzind, M., et al. 2008, A&A, 482, 67
Siebenmorgen, R., Haas, M., Krügel, E., & Schulz, B. 2005, A&A, 436, L5
Siebenmorgen, R., Heymann, F., & Krügel, E. 2011, in EAS Publications Series, Vol. 46, EAS Publications Series, ed. C. Joblin & A. G. G. M. Tielens, 285–290
Stalevski, M., Fritz, J., Baes, M., Nakos, T., & Popovic, L. C. 2011, ArXiv e-prints
Sturm, E., Hasinger, G., Lehmann, I., et al. 2006, ApJ, 642, 81
Sturm, E., Schweitzer, M., Lutz, D., et al. 2005, ApJ, 629, L21
Tristram, K. R. W., Meisenheimer, K., Jaffe, W., et al. 2007, A&A, 474, 837
van Bemmel, I. M. & Dullemond, C. P. 2003, A&A, 404, 1
van Loon, J. T., Groenewegen, M. A. T., de Koter, A., et al. 1999, A&A, 351, 559
Witt, A. N. 1977, ApJS, 35, 1